

## Supporting Information

### Counterion Distribution Surrounding Spherical Nucleic Acid-Au Nanoparticle Conjugates (SNA-AuNPs) Probed by Small Angle X-Ray Scattering (SAXS)

Sumit Kewalramani,<sup>†</sup> Jos W. Zwanikken,<sup>†</sup> Robert J. Macfarlane,<sup>‡,◇</sup> Cheuk-Yui Leung,<sup>§,△</sup> Monica Olvera de la Cruz,<sup>†,‡</sup> Chad A. Mirkin<sup>‡,†</sup> and Michael J. Bedzyk<sup>†,§,\*</sup>

<sup>†</sup> Department of Materials Science and Engineering, <sup>‡</sup>Department of Chemistry, <sup>§</sup>Department of Physics and Astronomy, Northwestern University, Evanston, Illinois 60208.

<sup>◇</sup>Present Address: Division of Chemistry and Chemical Engineering and Applied Physics Department, California Institute of Technology, Pasadena, California 91125.

<sup>△</sup>Present Address: Biogen Idec, Cambridge, Massachusetts 02142.

\*To whom correspondence should be addressed. Email: [bedzyk@northwestern.edu](mailto:bedzyk@northwestern.edu)

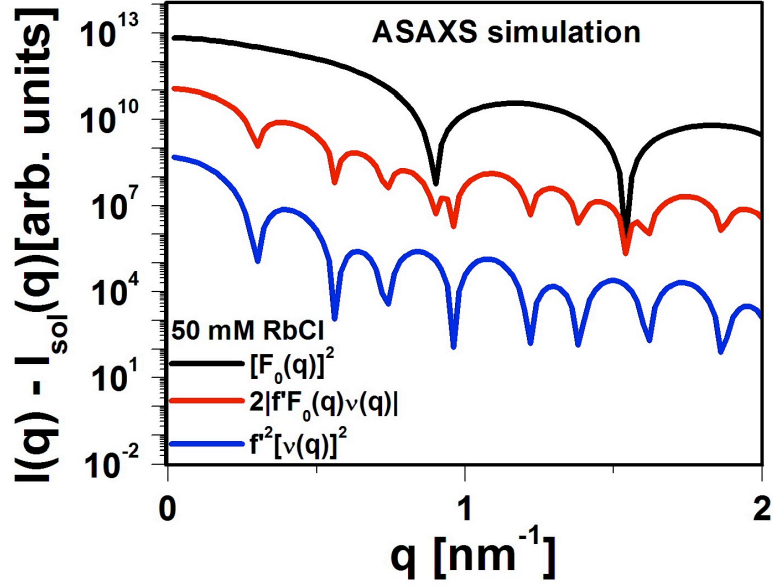


**Figure S1.** Calculation, based on equation S2, for the non-resonant (**black-line**) and resonant (**red-** and **blue-**lines) contributions to the SAXS intensity for 50 mM RbCl at X-Ray energy  $E = E_K - 3$  eV, where  $E_K = 15,200$  eV corresponds to the Rb K edge. The calculations are performed for RbCl because the K absorption edge for Rb is readily accessible at X-Ray synchrotron sources.

## I. ASAXS model calculations

Here we describe in our case study why ASAXS is not sufficiently sensitive for measuring the counterion distribution surrounding the SNA-Au nanospheres.

### Background and key result

Anomalous SAXS (ASAXS)-analysis of the counterion cloud structure relies on the measurements of the subtle X-Ray energy-dependent changes in the scattered intensity pattern from a polyelectrolyte-counterion system, which are induced by the sharp changes in the scattering strength (number of electrons)  $f_M$  of the counterion  $M^+$  occurring near a core-electron binding energy (absorption edge).<sup>1-4</sup>

$$f_M = Z_M + f_M'(E) + if_M''(E) \quad (S1)$$

For a counterion  $M^+$ ,  $Z_M$  is the number of electrons, and  $f_M'$  and  $f_M''$  are the real and imaginary parts of the dispersion correction.

To test the applicability of ASAXS for determining the distribution of counterions surrounding SNA-AuNPs, we carried out model calculations for SNA-AuNPs dispersed in 50 mM RbCl. In order to avoid strong fluorescence from the counterions, ASAXS measurements are typically performed at X-Ray energies below the absorption edge of the counterion. Under such conditions, the ASAXS effect is primarily determined by  $f'_M$ .<sup>4</sup> For the case of Rb<sup>+</sup>,  $f'_{Rb}$  changes from -1.4 to -10 in going from 2700 eV below the Rb K edge to 1 eV below the Rb K edge.<sup>4</sup> We have performed model calculations at an X-Ray energy 3 eV below the Rb K edge, where  $f'_{Rb} \sim -8$ .<sup>4</sup>  $f''_{Rb} = 0$  is assumed for these calculations. Following Dingemans *et al.*,<sup>3-4</sup> the X-Ray energy-dependent SAXS intensity for spherically symmetric SNA-AuNP-Rb<sup>+</sup> above the scattering due to the salt solution can be written as:

$$I(q, E) - I_{RbCl}(q, E) = [F(q)]^2 = [F_0(q)]^2 + 2f'_{Rb}F_0(q)v(q) + [f'_{Rb}v(q)]^2 \quad (S2)$$

Here,  $I(q, E)$  and  $I_{RbCl}(q, E)$  are the scattered intensities from the RbCl solution with and without SNA-AuNP, respectively.  $F_0(q)$  is the energy-independent, *i.e.* the non-resonant scattering amplitude from SNA-AuNP-Rb<sup>+</sup>, and can be assumed to be the measured scattered intensity far below the Rb K edge. For SNA-AuNPs,  $F_0(q)$  is largely determined by the strong X-Ray scattering Au core.  $v(q)$  is also energy independent and is the Fourier transform of the excess counterion concentration.

$$v(q) = 4\pi \int_0^{\infty} [n_{Rb}(r) - n_s] \frac{\sin(qr)}{qr} r^2 dr \quad (S3)$$

Here,  $n_{Rb}(r)$  is the distribution of Rb<sup>+</sup> in the presence of SNA-AuNP and  $n_s$  is the density of Rb<sup>+</sup> in the bulk solution far from SNA-AuNP. Figure S1 shows that at 3 eV below the Rb K edge, the scattered intensity due to the dominant X-Ray energy dependent term  $2|f'_{Rb}F_0(q)v(q)|$  is in general, two orders of magnitude lower than the non-resonant term  $[F_0(q)]^2$ . In particular at  $q = 0$ ,

$2|f'_{Rb}F_0(q)\nu(q)|/[F_0(q)]^2 \sim 0.016$ . These observations imply that in going from an X-Ray energy far below the Rb K edge to an energy just 3 eV below the Rb K edge, the scattered intensity from SNA-AuNP-Rb<sup>+</sup> changes merely by  $\sim 1.6\%$ . Such changes are typically close to the statistical uncertainties of the experiment. Therefore, ASAXS is not applicable to solving the distribution of counterions surrounding SNA-AuNPs. Details of the ASAXS model calculations are given below. The assumptions regarding the Au cores, the oligonucleotides and the cation distribution presented below are identical for ASAXS (Figure S1) as well as HIRSAXS model calculations (Figure 1B).

### Model

The scattering amplitude  $F(q)$  for spherically symmetric SNA-AuNP-Rb<sup>+</sup> can be written as:<sup>3-4</sup>

$$F(q) = 4\pi \int_0^{\infty} [\rho(r) - \rho_s] \frac{\sin(qr)}{qr} r^2 dr \quad (S4)$$

Here,  $\rho(r)$  and  $\rho_s$  are the electron densities for SNA-AuNP-Rb<sup>+</sup> and the RbCl salt solution respectively. Further,  $\rho_s$  can be written as

$$\rho_s = n_s(Z_{Rb} + f'_{Rb}) + n_s Z_{Cl} + (1 - V_{Rb}n_s - V_{Cl}n_s)\rho_w \quad (S5)$$

Here,  $n_s$  is the number density for Rb<sup>+</sup> as well as Cl<sup>-</sup> in bulk solution. For 50 mM RbCl,  $n_s = 0.03$  ions/nm<sup>3</sup>.  $V_{Rb}$  and  $V_{Cl}$  are the volumes of Rb<sup>+</sup> and Cl<sup>-</sup> ions that are calculated from the ionic Pauling radii (Table S1),  $Z_{Rb} = 36$ , and  $Z_{Cl} = 18$ , are the number of electrons for Rb<sup>+</sup> and Cl<sup>-</sup>,  $f'_{Rb} = -8$  is the anomalous dispersion correction to the Rb<sup>+</sup> scattering power at an X-Ray energy 3 eV below the Rb K edge, and  $\rho_w = 334$  e/nm<sup>3</sup> is the electron density for pure water.

To calculate  $\rho(r)$ , a simplified core-shell model for SNA-AuNP is used with an Au core of radius  $R = 5$  nm, and a thickness of the oligonucleotide shell  $t_{DNA} = 9.5$  nm. For the oligonucleotides used in the study,  $t_{DNA} = 9.5$  nm corresponds to an average rise of 0.34 nm per

base or base pair, consistent with the B-form of DNA in aqueous solutions.<sup>5</sup> Each oligonucleotide is assumed to be a cylindrical rod of radius  $1\text{nm}$ <sup>6</sup> and length  $t_{DNA}$ , and an electron density  $\rho_{DNA} = 460 \text{ e/nm}^3$ . The number of oligonucleotides/SNA-AuNP is chosen to be  $N_{DNA} = 70$ , roughly corresponding to the maximum loading of DNA on Au cores.<sup>7</sup> It is further assumed that  $\text{Rb}^+$  are uniformly distributed in the oligonucleotide shell and fully compensate the charge of the nucleic acids. Therefore, the number density of  $\text{Rb}^+$  in the oligonucleotide shell is  $n_{s/Rb} = N_{DNA} \times 46/V_{sh}$ . Where, 46 is the number of bases per oligonucleotide and  $V_{sh}$  is the volume of the shell. Finally, it is assumed that there are no  $\text{Cl}^-$  in the oligonucleotide shell. Under these assumptions  $\rho(r) - \rho_s$  is given by

$$\begin{aligned}
\rho(r) - \rho_s &= [(\rho_{Au} - \rho_w) - n_s \Delta f_{Cl}] - n_s \Delta f_{Rb} - n_s f'_{Rb} & r \leq R \\
&= [V_f (\rho_{DNA} - \rho_w) - n_s \Delta f_{Cl}] + [n_{s/Rb} - n_s] \Delta f_{Rb} + [n_{s/Rb} - n_s] f'_{Rb} & R < r \leq R + t_{DNA} \\
&= 0 & R > R + t_{DNA} \quad (S6)
\end{aligned}$$

Here,  $\rho_{Au} = 4660 \text{ e/nm}^3$  is the electron density for Au,  $V_f$  is the fraction of the SNA-AuNP shell volume occupied by the nucleic acids, and  $\Delta f_{Rb}$  and  $\Delta f_{Cl}$  are the renormalized contrast for the ions in water (defined in the main text, see also Table S1).

Note that the excess  $\text{Rb}^+$  concentration  $n_{Rb}(r) - n_s$  is given by

$$\begin{aligned}
n_{Rb}(r) - n_s &= -n_s & r \leq R \\
&= n_{s/Rb} - n_s & R < r \leq R + t_{DNA} \\
&= 0 & R > R + t_{DNA} \quad (S7)
\end{aligned}$$

Therefore, from equations S6 and S7, it can be shown that the form factor  $F(q)$  is composed of X-Ray energy independent and X-Ray energy-dependent terms :

$$F(q) = F_0(q) + f'_{Rb} \nu(q) \quad (S8)$$

This is an equivalent form of equation S2.

## II. Heavy ion replacement SAXS (HIRSAXS) model calculations

From equations S6 and S7, we note the  $F_0(q)$  can be further decomposed into counterion-dependent and counterion-independent scattering amplitudes

$$F_0(q) = F_{np}(q) + \Delta f_M \nu(q), \quad (\text{S9})$$

which is equivalent to

$$[F_0(q)]^2 = [F_{np}(q)]^2 + 2\Delta f_M F_{np}(q)\nu(q) + [\Delta f_M \nu(q)]^2 \quad (\text{S10})$$

Here,  $F_{np}(q)$  depends only on the scattering from SNA-AuNP, water and salt anions. The term  $[\Delta f_M \nu(q)]^2$  is neglected in equation 1 in the main text because it is 1-2 order lower in magnitude as compared to the other counterion-distribution-dependent term  $2\Delta f_M F_{np}(q)\nu(q)$ , which is linear in  $\Delta f_M$ . This observation is analogous to the ASAXS case (Figure S1), where the intensity term quadratic in  $f_{Rb}'$  is  $\sim 2$  orders of magnitude lower than the intensity term that is linear in  $f_{Rb}'$ .

As discussed in the main text, for SNA-AuNPs in 50 mM MCl, at  $q = 0$ , the contribution of the cation dependent term  $2\Delta f_M F_{np}(q)\nu(q)$  to the overall SAXS intensity was calculated to be 9.5%, 6.5%, 3.1% and 1.9% for M = Cs, Rb, K, Na, respectively. Similarly, for SNA-AuNPs in 30 mM solutions, at  $q = 0$ , the contribution of the cation dependent term to the overall SAXS intensity was calculated to be 10.0%, 6.9%, 3.3%, and 2.0% for M = Cs, Rb, K, and Na, respectively. As demonstrated in the main text, such changes are measurable above the uncertainties for our experiment.

The above observations imply that the scattered intensity increases by  $\sim 8.4\%$  (50 mM case) or  $\sim 8.9\%$  (30 mM case) when the ion in the solution is changed from  $\text{Na}^+$  to  $\text{Cs}^+$ . Therefore, the HIRSAXS is better than five-fold more sensitive than ASAXS for determining the

distribution of monovalent cations surrounding SNA-AuNPs. The reason is that in ASAXS the  $f'$  for  $\text{Rb}^+$  changes by  $\sim -7$ , when the incident energy is changed from 2700 to 3 eV below the Rb K edge. By contrast, under the heavy ion replacement approach, when the ion is changed from  $\text{Na}^+$  to  $\text{Cs}^+$ , the ion scattering power changes by  $\Delta f_{\text{Cs}} - \Delta f_{\text{Na}} \sim 38$ .

Finally, it should be noted that the uniform distribution model used in the above calculations is an over-simplification of the real cation distribution. However, at  $q = 0$ , the resonant intensity terms (second and third terms in equation S2, ASAXS) and the cation-species dependent intensity terms (second and third terms in equation. S10, HIRSAXS) depend upon the number of cations in the SNA-AuNP shell and not their exact radial distribution. Therefore, the model is expected to correctly predict, at  $q = 0$ , the contribution to the SAXS intensity due to these terms. Furthermore, the model correctly depicts (Figures 1B, and S1) that the periods for the sharp intensity modulations are shorter for the cation-dependent (HIRSAXS) or the resonant intensity terms (ASAXS) than for the cation-independent (HIRSAXS) or the non-resonant intensity (ASAXS). This qualitative picture is also independent of the model used in the calculations because the cation distribution is much more radially extended than the size of the Au cores.

### III. Effect of the ion size on its radial distribution around SNA-AuNPs

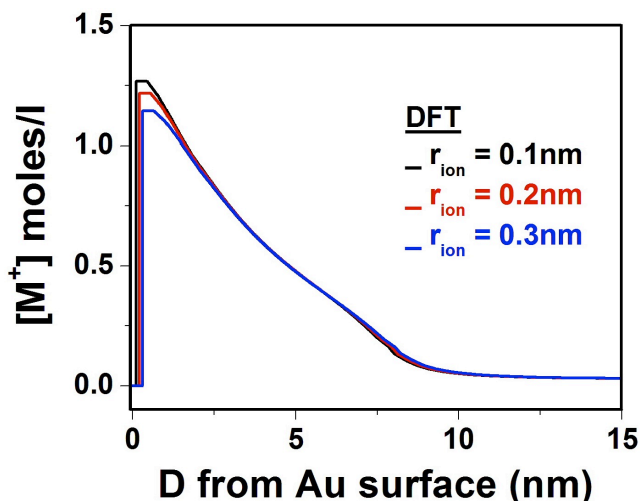


**Figure S2.** DFT-derived radial distribution profiles of cations surrounding SNA-AuNPs. The calculations are for cations of radius 0.1, 0.2 and 0.3 nm.

Figure S2 shows the distribution of cations surrounding SNA-AuNPs as a function of distance from the Au surface, for three different cation radii. The range of the cation radii (0.1-0.3 nm) used in DFT calculations encompasses the range of the cation radii in the experiments (Table S1). Figure S2 shows that in the close proximity of the Au surface, the cation concentrations differ by as much as  $\sim 9\%$ . Additionally, it is evident that in the narrow region ( $\sim 1$  nm) close to the Au surface, the cation density decreases with increasing cation size. Further out, the cation distribution profiles are nearly indistinguishable. Therefore, the underlying HIRSAXS assumption that the distribution of cations surrounding SNA-AuNPs does not depend upon the cation size is valid for distances greater than 1 nm from the Au surface. Even close to the Au surface, the assumption is a good approximation.

The DFT-derived ion size effect on the cation distribution is qualitatively consistent with intuitive expectations. Namely, the DNA packing density is maximal at the Au surface, and falls off as  $1/r^2$ . The cation distribution profiles are expected to roughly exhibit the same trends

because cations are expected to compensate the DNA charge. Therefore, the excluded volume effect on cations is expected to be most prominent in the vicinity of the Au surface.

Even close to the Au surface, the cation distribution does not depend very strongly on the cation size. The reason for this can be qualitatively understood by considering the average SNA-AuNP characteristics and the cation sizes. The SNA-AuNPs are comprised of Au cores with radius  $R = 4.5$  nm. Each AuNP is covered by 55 DNA strands (section VII below). If DNAs are assumed to be cylinders of radius  $1\text{nm}^6$  then the estimated fractional volume occupied by the DNAs is  $\sim 61\%$  and  $\sim 42\%$  in  $0.5$  nm thick spherical shells next to the Au surface and at a distance of  $1$  nm from the Au surface, respectively. Within the same spherical shells, DFT calculations suggest that the cations of radius  $0.3$  nm should occupy  $7.8\%$  and  $7.4\%$  of the volume. These observations imply that steric factors should not impose very strong restrictions on the distribution of cations surrounding SNA-AuNPs.

#### IV. Ion characteristics

**Table S1.** Pauling radii and renormalized contrast for the ions used in the study.

Ion	Pauling radius (nm)	$Z_M$	$\Delta f_M = Z_M - V_M \rho_w$
$\text{Na}^+$	0.102 <sup>a,c</sup>	10	8.51
$\text{K}^+$	0.138 <sup>a,c</sup>	18	14.32
$\text{Rb}^+$	0.148 <sup>a,d</sup>	36	31.46
$\text{Cs}^+$	0.174 <sup>b,c</sup>	54	46.62
$\text{Cl}^-$	0.181 <sup>a,e</sup>	18	9.70

<sup>a</sup> Coordination number = 6, <sup>b</sup> Coordination number = 8. The coordination number for a metal cation is chosen to be the same as in the corresponding metal chloride salt. The Pauling radii are the values listed in <sup>c</sup>reference 8, <sup>d</sup> reference 4 and <sup>e</sup> reference 9.

## V. Cation-distribution-dependent intensity $I_{cat}(q)$

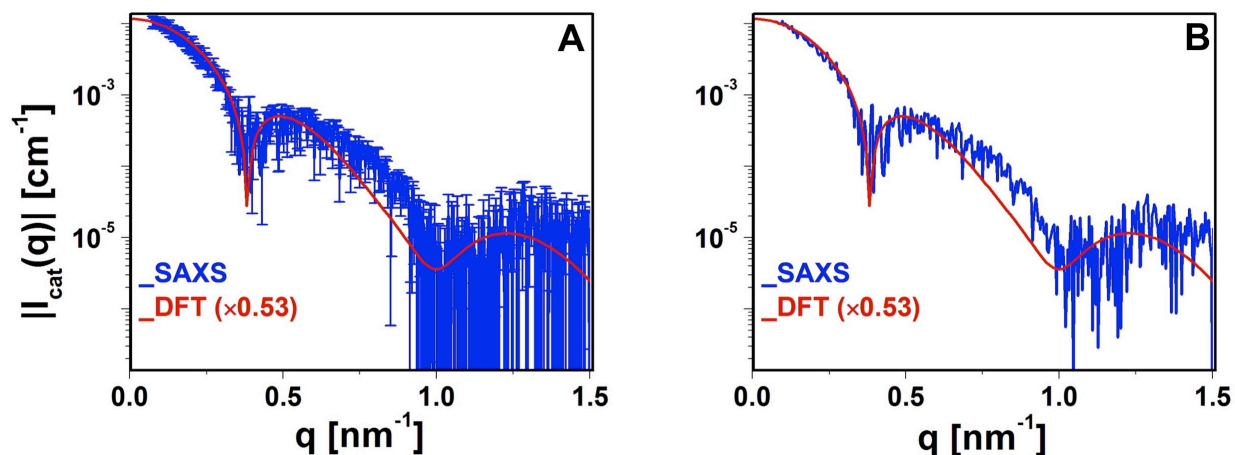


**Figure S3.** Comparison between SAXS-extracted and DFT-derived  $I_{cat}(q)$  for SNA-AuNPs in 30 mM MCl solutions. The figure (B) is same as (A) except that the uncertainties associated with SAXS-extracted  $I_{cat}(q)$  are not shown. In (A), for data points where the uncertainties on  $I_{cat}(q)$  were greater than 100%, the uncertainties have been manually lowered to be 99% of the mean values so that the error bars are visible on the log scale.

The data in the main text (Figure 2) were truncated at  $q = 0.8 \text{ nm}^{-1}$  because the uncertainties for  $I_{cat}(q)$  are excessively large above this  $q$ . Here, we show  $I_{cat}(q)$  up to  $q = 1.5 \text{ nm}^{-1}$ , for SNA-AuNPs in 30 mM MCl. Figures S3A and S3B show  $I_{cat}(q)$  with and without the associated uncertainties, respectively. For comparison, the DFT-derived intensities are also shown. These figures show very reasonable shape agreement between the DFT-calculated and the SAXS-derived  $I_{cat}(q)$  over the extended experimental  $q$  range.

## VI. Fitting of SAXS-extracted $[F_{np}(q)]^2$

The SAXS-extracted  $[F_{np}(q)]^2$  is fitted with a simplified model based on core-shell description of SNA-AuNPs, described above. The DNAs are treated as cylindrical rods of radius 1 nm and a length equivalent to SNA shell thickness  $t_{DNA}$  and an average electron density  $\rho_{DNA}$ .  $t_{DNA}$  and  $\rho_{DNA}$  are fitting parameters in the model. The anions in the SNA shell are neglected in

these calculations. The radial electron density for the SNA shell is resulting angular-averaged density based on this model. In this section, we describe why such a simplified model is valid.

$[F_{np}(q)]^2$  is dominated by Au core scattering and exact structural features of DNA as well as the anion distribution are difficult to extract. To illustrate, we estimate the effective number of electrons that contribute to scattering from the Au core, DNA and the anions in the SNA shell. For the DNA and the Au core, the effective number of electrons are calculated as  $Z_{eff} = V(\rho - \rho_w)$ . Here,  $V$  and  $\rho$  are the volume and the electron density of the Au core or the DNA.  $\rho_w$  is the electron density for water. For  $\text{Cl}^-$ , the effective number of electrons are calculated as  $\Delta f_{Cl} \times N_{s/cl}$ , where  $\Delta f_{Cl}$  is the effective number of electrons per  $\text{Cl}^-$  (Table 1) and  $N_{s/cl}$  is the number of  $\text{Cl}^-$  in the SNA shell. For  $R = 4.5$  nm Au core (the mean size), the effective number of electrons/Au core are  $\sim 1.65 \times 10^6$ . By contrast, the mean electron density for DNA ( $435 \text{ e/nm}^3$ ) extracted from the model predicts the effective number of electrons per DNA strand to be 2601. There are 55 DNA/Au core. Therefore, the total number of electrons for the DNA that contribute to scattering are  $\sim 1.43 \times 10^5$ . The concentration of the anions in the SNA shell is expected to be much less than in bulk solution because DNA are negatively charged. Even assuming the bulk solution concentration of anions (30 mM) in the SNA shell gives the effective number of electrons for all the  $\text{Cl}^-$  in the SNA shell (combined) to be  $4.8 \times 10^4$ , which is less than 3% of the corresponding value for the Au core. For this reason, we have not discussed the anion distribution in the SNA shell.

Despite the above mentioned difficulties, the mean electron density for DNA ( $435 \text{ e/nm}^3$ ) predicted by the simplified model is reasonable because it implies that the effective number of electrons for the DNA are 2601, compared to  $Z$  number of 7320 in vacuum. This result is in good qualitative agreement with a previous SAXS study on short double-stranded DNA in aqueous

solutions.<sup>2</sup> This study found that for a DNA with  $Z = 8500$  in vacuum, the effective number of electrons in the aqueous solution were reduced to  $2600 \pm 500$ . The length of the DNA (8.2 nm) extracted from this model is also reasonable, as validated by comparisons between SAXS-extracted and theoretical model calculations for  $I_{cat}(q)$ . Finally, note that the  $t_{DNA}$  and  $\rho_{DNA}$  are extracted under the assumption of maximum loading of Au nanoparticles by DNA. As discussed above, the fit-extracted parameters correctly predict the effective number of electrons for the DNA. Therefore, the underlying “maximum-loading” assumption should be valid.

## VII. Dependence of the number of oligonucleotides on the Au core size.

The Au nanoparticles used in the preparation of SNA-AuNPs are polydispersed. Therefore, the SAXS-extracted cation-distribution-dependent and cation-independent scattered intensities are averaged over the SNA-AuNP size distribution. Previous studies have shown that the number of oligonucleotides/SNA-AuNP,  $N_{DNA}$ , depends on the Au core size.<sup>7, 10</sup> It should be noted that the cation distribution surrounding SNA-AuNPs depends upon  $N_{DNA}$ , which determines the total charge on SNA-AuNP. Therefore, to theoretically model the polydispersity-averaged SAXS intensities, and thereby extract the cation distribution surrounding SNA-AuNPs, the changes in  $N_{DNA}$  as a function of Au core size need to be taken into account. The relevant Au core sizes are  $R \sim 3-6$  nm because the mean size of the Au cores is  $\langle R \rangle \sim 4.5$  nm and the polydispersity is  $\sim 8.5\%$  (Table 1, main text). Figure S4A shows that over (and near) this range of the Au core sizes, the minimum projected area of the oligonucleotide onto the Au core (footprint)<sup>7</sup> scales as  $\sqrt{R}$ . Specifically, footprint =  $4.9 \times \sqrt{(R/5)}$ , where  $4.9 \text{ nm}^2$  is the oligonucleotide footprint for Au core of  $R = 5$  nm. Therefore,  $N_{DNA}(R) = 4\pi R^{3/2}/2.19$ , as shown in Figure S4B.

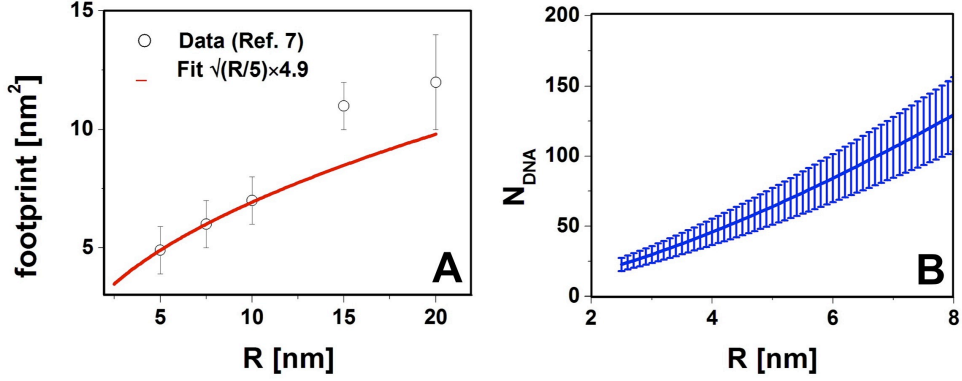


**Figure S4.** (A) Minimum area/oligonucleotide as a function of the Au core size (data taken from reference 7) and the corresponding fit. (B) Calculated number of oligonucleotides per SNA-AuNP based on the functional form of the fit in (A).

### VIII. Effect of salt concentration on cation distribution surrounding SNA-AuNP

As mentioned in the main text, no significant differences are expected or observed in the counterion distribution for SNA-AuNP in 30 and 50 mM MCl solutions. Specifically, the inherent spatial resolution,  $\pi/q_{\max} = 3.9$  nm, cannot discriminate subtle changes caused by these concentration differences. For example, the counterion cloud extent beyond the SNA shell as characterized by the Debye length should be  $\kappa^{-1} = 1.75$  and 1.36 nm for the cases of 30 and 50 mM MCl, respectively. The 0.39 nm difference is much smaller than the aforementioned resolution. Therefore, despite having two different concentrations, the two data sets are equivalent. To elaborate *via* a direct comparison, we replot for the two cases, the DFT-based  $I_{cat}(q)$  shown in Figures 4B-C in Figure S5A. The SAXS-extracted  $I_{cat}(q)$  for the two cases are shown in Figure S5B. It should be noted that for the 50 mM case, the concentration of SNA-AuNPs was 80 nM, in contrast to 70 nM SNA-AuNPs used for the 30 mM case. Further note that  $I_{cat}(q)$ , are obtained as the slopes of the best-fit lines through the  $\Delta I_M$  vs  $\Delta f_M$ , at each  $q$ . Therefore,  $I_{cat}(q)$  are directly proportional to the number of SNA-AuNPs or the SNA-AuNP concentration. Therefore, in Figure S5, to take into account the differences in SNA-AuNP

concentrations, the simulated and the SAXS-extracted  $I_{cat}(q)$  for SNA-AuNPs in 50 mM MCl are multiplied by 0.875 (7/8). Figure S5B clearly shows that within the associated uncertainties and for the limited  $q$ -range of the experimental  $I_{cat}(q)$ , the two data sets are nearly equivalent. The DFT-derived intensities  $I_{cat}(q)$  for the two cases are also nearly equivalent. Because  $I_{cat}(q) = 2F_{np}(q)v(q)$ , the above observations imply that there are no significant differences that can be detected in the DNA conformation and the cation distribution surrounding SNA-AuNPs between the cases of SNA-AuNPs in 30 and 50 mM MCl.

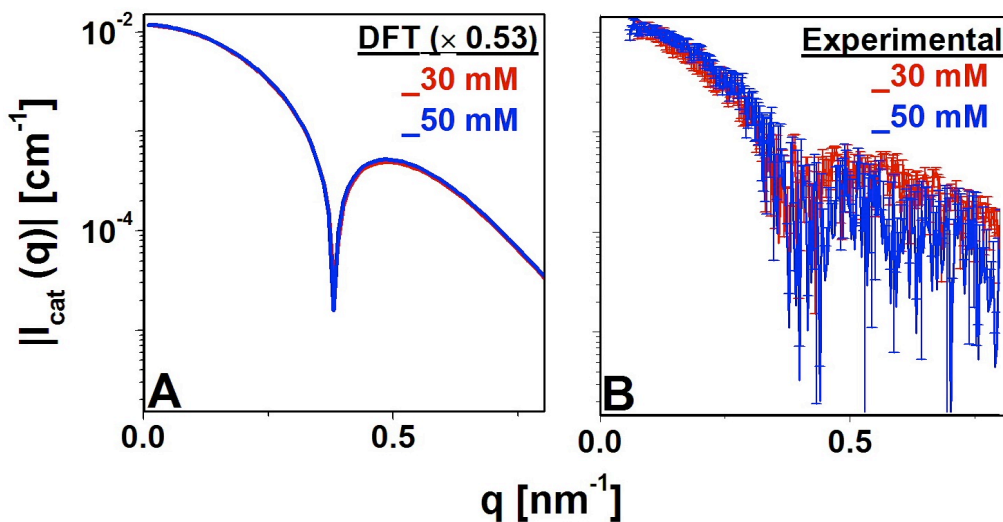


**Figure S5.** (A) DFT-based and (B) SAXS-extracted  $I_{cat}(q)$  for SNA-AuNP in 30 and 50 mM MCl. The data have been normalized to take into account the differences in the SNA-AuNP concentration between the 30 and 50 mM MCl cases (see text above).

### IX. Melting temperature of double stranded DNA segments

Baldino *et al.* show that the melting temperature for duplexes in NaCl can be estimated as  $T_m = 81.5 + 16.6\log([Na^+]) + 0.41[\%(G + C)] - 675/N_{bp}$ .<sup>11</sup> Here,  $N_{bp}$  is the number of base pairs in the duplex and  $\%(G + C)$  is the percentage fraction of the G-C base pairs in the duplex. We have used  $[Na^+] = 0.45$  M, which is the average cation concentration in the SNA shell to estimate

$T_m = 49.6$  °C, for the duplexes used. The  $T_m$  is consistent with a more detailed and sophisticated analysis for the chain-length dependence of melting temperatures.<sup>12</sup>

### X. DFT-derived $I_{cat}(q)$ for different sizes of the cation

In order to examine the effects of cation size on the cation-distribution-dependent intensity, DFT calculations were performed for three different cation radius; 0.1, 0.2, and 0.3 nm, and for the case of SNA-AuNP in 30 mM MCl. For each cation size, the DFT calculations for cation distribution were performed for Au core sizes ranging from 2.6 to 7.0 nm, for polydispersity averaging. Comparisons between theoretical polydispersity-averaged  $I_{cat}(q) = 2\langle F_{np}(q)v(q) \rangle$  and the experimental  $I_{cat}(q)$  are shown in Figure S6. In Figure S6, for each cation size, the theoretical  $I_{cat}(q)$  has been multiplied by the same scale factor  $SF = 0.53$ . Figure S6 clearly shows that over the  $q$ -range for which the SAXS-derived  $I_{cat}(q)$  can be reliably extracted,  $I_{cat}(q)$  does not depend sensitively on the size of the cation. This validates the HIRSAXS approach.

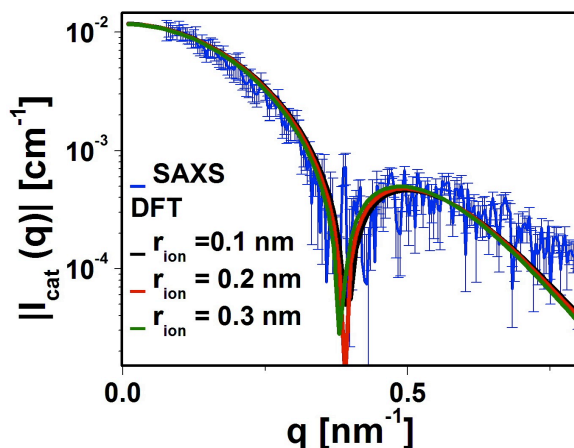


**Figure S6.** DFT-derived  $I_{cat}(q)$  for cation radii of 0.1, 0.2 and 0.3 nm are compared with the SAXS-extracted  $I_{cat}(q)$  for SNA-AuNPs in 30 mM MCl.

## XI. Geometric models for cation distribution

The limited  $q \leq 0.8 \text{ nm}^{-1}$  range for  $I_{cat}(q)$  implies a low spatial resolution for sensing the counterion distribution. Therefore, the DFT-derived cation density profiles (Figure 4A, main text) may not be unique solutions for the distribution of cations surrounding SNA-AuNPs. Therefore, the key question is: can the limited  $q$ -range SAXS data for  $I_{cat}(q)$  distinguish between different cation distributions? To answer this question and to gain insight into the model-independent features of the distribution of cations surrounding SNA-AuNPs that may be extracted from the limited  $q$ -range data, the SAXS-derived  $I_{cat}(q)$  are also compared to intensities from simplified geometric models for cation distribution.

Figure S7A shows a cation distribution  $n_{DNA}(r)$  (green trace), which follows the charge density of the DNA. In other words, the model assumes that each negative charge on the oligonucleotide is neutralized by a corresponding monovalent cation. Furthermore, the cations are located at the same radial distances as the negative charges on the nucleic acid backbone. The DNA model used for these calculations was identical to that used in DFT. Similar to the case for DFT, the cation distributions with this simplified model were calculated for Au core sizes ranging from 2.6 nm to 7.0 nm, for polydispersity-averaging.

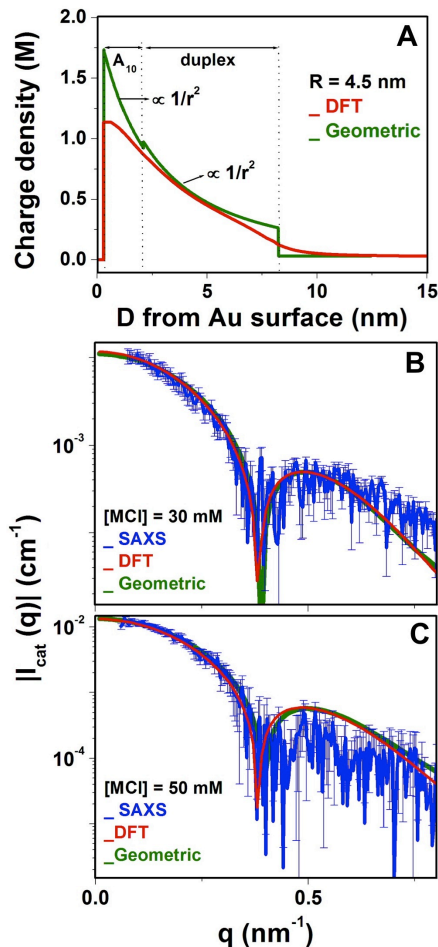


**Figure S7.** SAXS-extracted, DFT-derived and geometric-model-derived cation-distribution-dependent intensities. (A) For SNA-AuNPs in 30 mM MCl, the DFT-derived  $n_{+DFT}(r)$  and the geometric model-derived  $\text{Na}^+$  distribution as a function of distance from the Au surface (red and green curves). (B) Comparisons between the SAXS-extracted and the DFT- and the geometric-model-derived  $|I_{cat}(q)|$  for SNA-AuNPs in 30 mM MCl, and (C) 50 mM MCl.

Figures S7B and S7C show the polydispersity-averaged  $I_{cat}(q)$  based on the geometric model along with the SAXS-extracted and the DFT-derived  $I_{cat}(q)$ , for the cases of SNA-AuNPs in 30 mM and 50 mM MCl solutions, respectively. Figures S7B-C show that the simple geometric model is an equally good description of the experimental  $I_{cat}(q)$  as the DFT. However, it must be mentioned that in order to quantitatively match the SAXS-extracted  $I_{cat}(q)$ , the theoretical intensity from the geometric model had to be multiplied by a scale factor of 0.49, which is slightly lower than the  $SF = 0.53$  for the DFT. Note that the DFT predicts that cations

compensate  $\sim 87\%$  of the DNA charge, whereas the simplified model predicts 100% of the DNA charge. If our interpretation that the hydration effects account for the  $SF (= 1/0.53)$  were true, the scale factor of 0.49 for the geometric model corresponds to  $\sim 92\%$  of the DNA charge compensated by the cations, which is close to the DFT-prediction. These observations imply that both these models predict close to, but slightly less than one cation per DNA charge.

It is clear that with the current experimental resolution, we cannot distinguish between the DFT-derived and the simple geometric models for cation distribution, as long as the DNA conformation used for the two models is identical. A practical implication of this observation is that we can simply use different DNA charge densities as cation distributions to test the accuracy of the oligonucleotide model used in DFT and the above-described geometric model. First, we show that the experimental  $I_{cat}(q)$  can be used to discriminate between slightly different cation distribution profiles. Thereafter, we vary systematically the DNA charge densities, and hence the cation distribution profiles to estimate the range of cation distributions (or DNA conformations) that can suitably describe the SAXS-derived  $I_{cat}(q)$ .

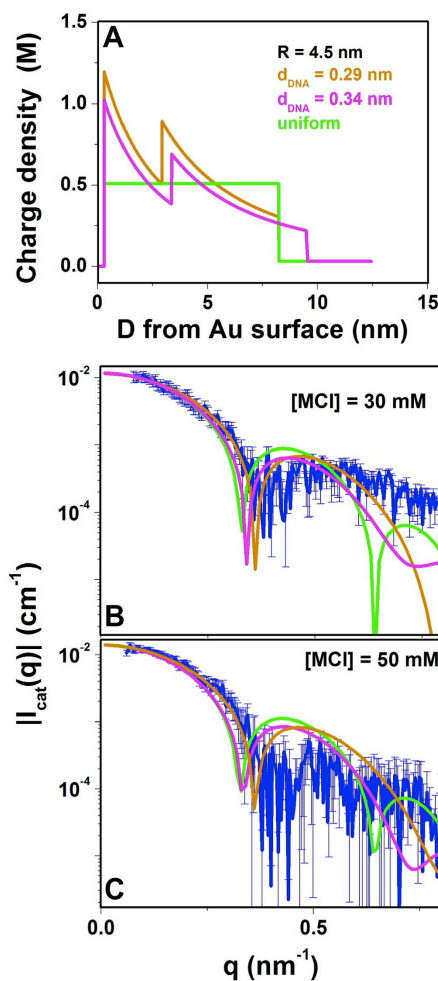


**Figure S8.** (A) Simplified models for cation distributions for SNA-AuNPs in 30 mM MCl. A uniform distribution of cations in the SNA shell (**green curve**), cation distributions similar to the DNA charge densities, but calculated using  $d_{DNA} = 0.34$  nm (**magenta curve**) and 0.29 nm (**orange curve**). (B) Comparison between the SAXS-derived and simplified model-derived  $|I_{cat}(q)|$  for SNA-AuNPs in 30 mM MCl and (C) 50 mM MCl. The model-derived  $|I_{cat}(q)|$  in (B) and (C) are color coded to match the color used for the cation distribution profile in (A).

Figure S8A shows two such test models. In case one (magenta curve), the inter-base and inter-base-pair distances for both the ss- and the ds-DNA segments are chosen to be  $d_{DNA} = 0.34$  nm, similar to the case of B-DNA conformation in aqueous solutions.<sup>5</sup> In the second case (orange curve), the SNA shell thickness is the same as that used in DFT calculations ( $t_{DNA} = 8.2$  nm). However, the inter-base and inter-base pair separations for the ss- and ds-DNA segments are assumed to be identical ( $d_{DNA} = 0.29$  nm). Finally, a theoretical intensity derived from a

uniform cation distribution (green trace) in the SNA shell ( $t_{DNA} = 8.2$  nm) is compared to experimental intensity, to show that an entirely unphysical cation distribution cannot suitably describe the SAXS-extracted  $I_{cat}(q)$ .

Figures S8B and S8C show a comparison of the intensities derived from these models and the SAXS-extracted  $I_{cat}(q)$ . Figures S8B-C show that both the uniform distribution profile and the cation distribution profile based on  $d_{DNA} = 0.34$  nm ( $t_{DNA} = 9.5$  nm) do not suitably describe the experimental  $I_{cat}(q)$ . This is because the simulated intensities from these models predict the position of the first minima at  $q \sim 0.33$  nm<sup>-1</sup>, as opposed to  $q \sim 0.38$  nm<sup>-1</sup> in the experimental data. Further, an additional minima at  $q = 0.65$  nm<sup>-1</sup> (uniform distribution, green traces) and  $q = 0.75$  nm<sup>-1</sup> ( $t_{DNA} = 9.5$  nm, magenta traces) is predicted by these models. More importantly, the cation distribution based on oligonucleotides with a uniform  $d_{DNA} = 0.29$  nm is also not a suitable model. For  $q > 0.5$  nm<sup>-1</sup>, the intensity based on this model (orange traces, Figures. S8B-C) drops-off much more steeply than the experimental  $I_{cat}(q)$ . These observations suggest that the limited  $q$ -range  $I_{cat}(q)$  profile is sensitive (with an accuracy of  $\sim 1$  nm) to the overall extent of the SNA-shell as well as the lengths of the ss- and ds-DNA segments.

For a detailed analysis of DNA configurations, we calculated polydispersity-averaged  $I_{cat}(q)$  for the case of SNA-AuNP in 30 mM MCl by systematically varying the length of the single-stranded DNA component  $L_{ss}$  from 1.0 nm to 3.4 nm in steps of 0.2 nm, and the length of the double-stranded DNA segment  $L_{ds}$  from 3.6 nm to 6.0 nm in steps of 0.4 nm. Additional calculations were done for  $L_{ds} = 6.1$  nm, which corresponds to rise/base-pair of 0.34 nm. The corresponding range of rise per base for the single-stranded component is 0.10 - 0.34 nm. Similarly, the rise per base pair the double-stranded segment varies from 0.20 to 0.34 nm. Two constraints were used. First, the rise/base-pair for the double-stranded segment was greater than

the rise/base for the single-stranded segment. Second, the thickness of the short thiol linker was fixed at 0.3 nm. For comparison with the SAXS-derived  $I_{cat}(q)$ , the simulated  $I_{cat}(q)$  were scaled appropriately such that the two intensity profiles matched exactly at  $q = 0.1 \text{ nm}^{-1}$ . The goodness of overall match of the two profiles was estimated from weighted  $\chi^2$ , defined as:

$$\chi^2 = \frac{1}{n} \sum_{i=1}^n \frac{(I_{cat/SAXS,i}(q) - I_{cat/sim,i}(q))^2}{\sigma_i^2} \quad (\text{S11})$$

Here,  $n$  is the number of data points for  $q \leq 0.8 \text{ nm}^{-1}$  for the SAXS-extracted  $I_{cat}(q)$  and  $\sigma_i$  are the uncertainties at each of these data points. Because of the large uncertainties in the experimental data, a stringent criterion for a reasonable match was used. Specifically, simulated  $I_{cat}(q)$  that matched the SAXS-extracted  $I_{cat}(q)$  with  $\chi^2 \leq 3.5$  were deemed to be suitable fit for the experimental data.

Figure S9A shows the variation of  $\chi^2$  as a function  $L_{ss}$  and  $L_{ds}$ , and Figure S9B shows SAXS-extracted  $I_{cat}(q)$  along with two simulated intensity profiles that were considered as reasonable match. Figure S9A shows that a reasonable agreement can be found for  $L_{ss}$  varying between 1.4 nm and 2.2 nm, and  $L_{ds}$  varying between 5.2 nm to 6.1 nm. The overall thickness of the DNA shell  $t_{DNA}$  was found to have a range 7.3 – 8.6 nm. It should be noted that the simulated  $I_{cat}(q)$  profile shown in Figure S7B is the best match for the experimental  $I_{cat}(q)$  with a  $\chi^2 = 2.9$ . This intensity profile was derived with  $L_{ss} = 1.8 \text{ nm}$  and  $L_{ds} = 6.1 \text{ nm}$ , corresponding to 0.18 nm rise/base for the single-stranded segment and 0.34 nm rise/base-pair for the double-stranded segment of the DNA.

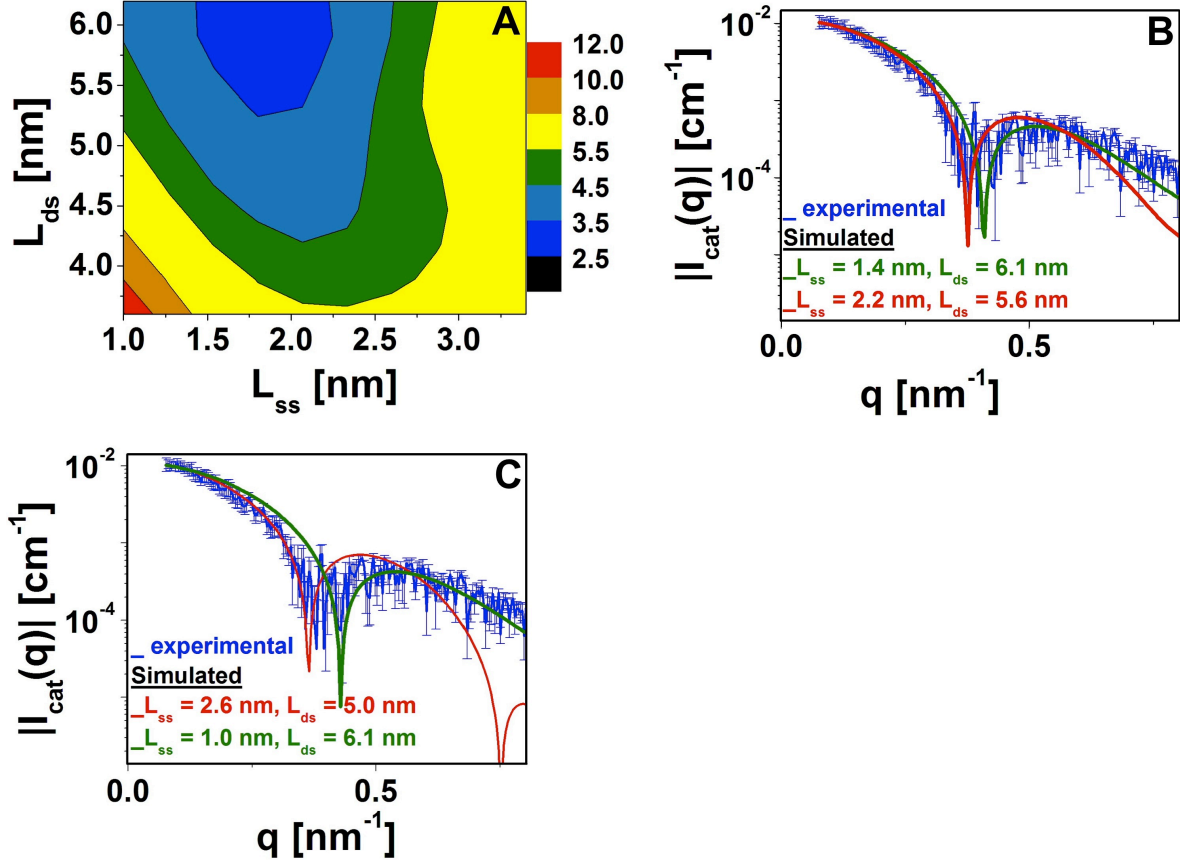


**Figure S9.** (A) 2D contour plot of  $\chi^2$  as a function of  $L_{ss}$  and  $L_{ds}$ . (B) Examples of simulated  $|I_{cat}(q)|$  that reasonably match the SAXS-extracted  $|I_{cat}(q)|$ . The calculated  $\chi^2$  for  $|I_{cat}(q)|$  derived using  $L_{ss} = 1.4$  and  $L_{ss} = 2.2$  nm are 3.5 and 3.3, respectively. (C) Examples of simulated  $|I_{cat}(q)|$  that do not reasonably match the SAXS-extracted intensity. The calculated  $\chi^2$  for  $|I_{cat}(q)|$  derived using  $L_{ss} = 1.0$  and  $L_{ss} = 2.6$  nm are 4.4 and 4.9, respectively.

Figures S9C provide examples for justification of the criterion  $\chi^2 \leq 3.5$ . Specifically, Figure S9C shows the SAXS-extracted  $I_{cat}(q)$  along with two simulations with  $\chi^2 = 4.4$  and 4.9. The simulation with  $L_{ss} = 1.0$  nm ( $\chi^2 = 4.4$ ) deviates from the SAXS-derived  $I_{cat}(q)$  at low  $q$ , and shows a minima position at  $q = 0.42$  nm<sup>-1</sup>, slightly higher than the minima position of  $q \sim 0.38$  nm<sup>-1</sup> in the SAXS-extracted  $I_{cat}(q)$ . By contrast, the simulation with  $L_{ss} = 2.6$  nm ( $\chi^2 = 4.9$ ) shows a much steeper drop in intensity, and an additional oscillation at high  $q$ .

We have shown only one example illustrating the equivalence of DFT and the geometric model (Figures S7B-C). However, we have tested this assumption by doing two other

comparative simulations for DNA configurations:  $L_{ss} = 1.4$  nm with  $L_{ds} = 6.0$  nm and  $L_{ss} = 2.6$  nm with  $L_{ds} = 5.0$  nm. No substantial differences between the two approaches were found. Finally, we note that on the basis of the current data, we cannot distinguish between the DFT-derived  $n_{+DFT}(r)$  and the geometric model-derived  $n_{DNA}(r)$  cation distributions that best describe the experimental  $I_{cat}(q)$ . Nevertheless, we note that  $n_{+DFT}(r)$  is the more plausible cation-distribution profile. This is because the very sharp osmotic gradients in the ion density profile, such as those predicted by  $n_{DNA}(r)$  are unphysical.

## XII. Data processing

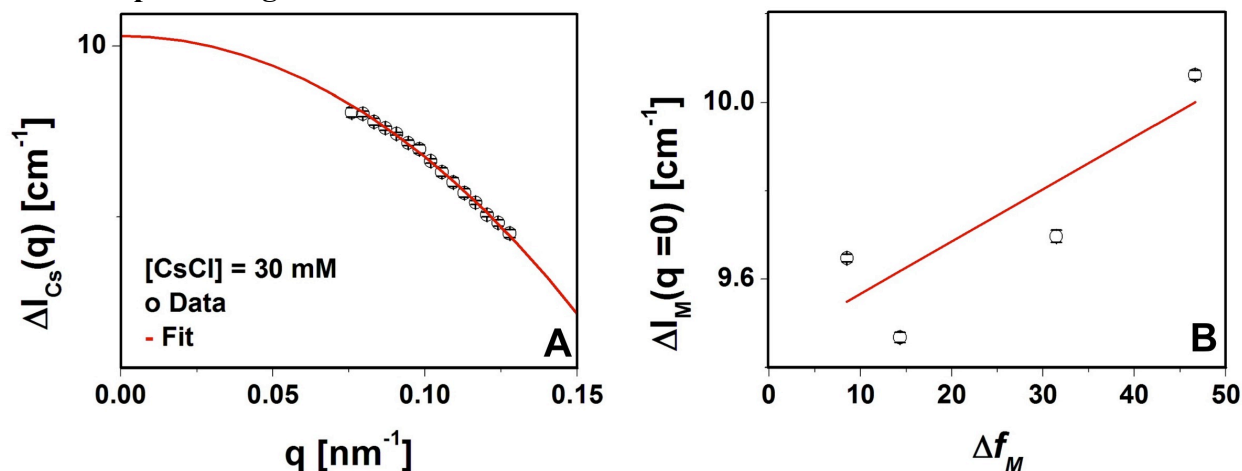


**Figure S10.** Rescaling the measured scattered intensities from SNA-AuNPs dispersed in MCl ( $M = \text{Na}, \text{K}, \text{Rb}$  or  $\text{Cs}$ ) solutions. (A) Low  $q$  data (**black circle**) from SNA-AuNPs in 30 mM CsCl along with the corresponding fit (**solid red line**) based on the  $q \rightarrow 0$  form of the scattered intensity from spherical objects. (B) The scattered intensities from SNA-AuNPs in MCl solutions at  $q = 0$  (**black circle**) as a function of the effective number of electrons for each cation, along with the linear fit to the data (**solid red line**).

There were 4 sets of samples [2 each for SNA-AuNPs in 30 mM and 50 mM MCl; ( $M = \text{Na}, \text{K}, \text{Rb}$  or  $\text{Cs}$ )]; making 16 samples altogether. For 2 of the 4 sets, the very low- $q$  measured scattered intensity for SNA-AuNPs in NaCl was higher than that in KCl, *i.e.*  $\Delta I_{Na} > \Delta I_K$ . This observation is in contradiction to the expected monotonic increase in the scattered intensity with increasing number of electrons for the cation (Equation S10). It should be noted that at  $q = 0$ , the differences  $\Delta I_K - \Delta I_{Na}$  are expected to be very small ( $\sim 1.5\%$ ). Therefore, it is very likely that

the observed reversal in the order of the measured SAXS intensities is due to small errors in preparation of SNA-AuNP solutions. It should also be mentioned that for all the four sets of samples, and for low  $q$ , the intensities for SNA-AuNPs in RbCl and CsCl solutions were higher than the intensities from either SNA-AuNPs in NaCl or SNA-AuNPs in KCl solutions, and as expected,  $\Delta I_{Cs} > \Delta I_{Rb}$  was observed for all samples. To correct for the small errors in the preparation of SNA-AuNP dispersions, the measured SAXS intensities were rescaled separately for each of the four sets of samples, as follows. First, the low  $q$  intensities  $\Delta I_M$  for all cations were fitted to  $[A - B(q^2/10)]^2$ , which is the  $q \rightarrow 0$  form of the SAXS intensity from spherically symmetric objects (see note below).<sup>13</sup> Figure S10A shows an example of such a fit for 70 nM SNA-AuNPs in 30 mM CsCl, which is one of the samples described in the main text. Similarly good fits were achieved for SNA-AuNPs in the other metal chloride salts. Second, the fit-derived intensities at  $q = 0$ ,  $\Delta I_M(q = 0)$  are plotted against  $\Delta f_M$  and fitted by a line (Figure S10B). The SAXS intensities for each sample set were multiplied by a correction factor such that  $\Delta I_M$  matches the fitted line value at  $q = 0$ . For 70 nM SNA-AuNPs dispersed in 30 mM MCl described in the main text, the multiplicative factors for  $\Delta I_M$  are 0.990, 1.016, 1.013 and 0.994 corresponding to  $M = \text{Na, K, Rb and Cs}$ , respectively. Note that the multiplicative factors are derived from fitting the  $\Delta I_M(q = 0)$  data, which depend only on the total number of electrons in the SNA-AuNP- $M^+$  system and hence largely on the concentration of SNA-AuNPs in solutions. Therefore, the multiplicative factors suggest that for the as prepared solutions of SNA-AuNPs in NaCl,  $[\text{SNA-AuNP}] = 70.7 \text{ nM}$  and for SNA-AuNPs in KCl,  $[\text{SNA-AuNP}] = 68.9 \text{ nM}$ , instead of the expected 70.0 nM for both solutions. Similar analysis for the second sample described in the main text, *i.e.*, the 80 nM SNA-AuNPs dispersed in 50 mM MCl solutions, yield multiplicative factors 0.995, 1.005, 1.004 and 0.995 for  $M = \text{Na, K, Rb and Cs}$ , respectively.

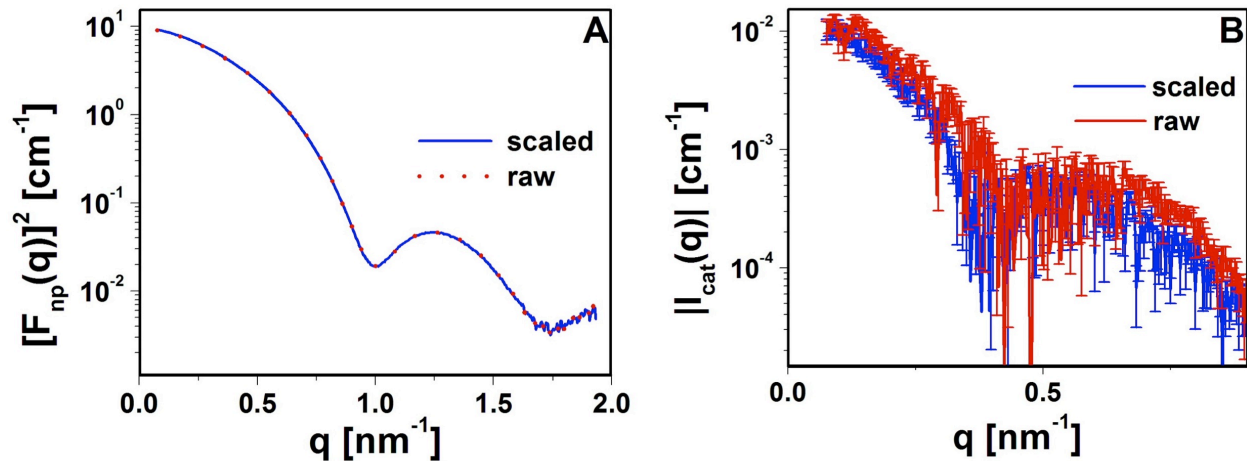


**Figure S11.** (A) The cation-independent SAXS intensity from scaled (solid black line) and unscaled (dotted red line), data. (B) The cation-distribution-dependent SAXS intensity derived from scaled (solid blue line) and unscaled (solid red line) data.

To show that this rescaling of the measured SAXS intensities does not have a significant effect on the results presented in the main text, comparison between cation-independent  $[F_{np}(q)]^2$  and cation distribution-dependent  $I_{cat}(q)$  extracted from scaled and un-scaled data are shown for SNA-AuNPs in 30 mM MCl in Figure S11. Figure S11A shows that the cation independent intensities are nearly identical whether scaled or un-scaled data is used. For  $|I_{cat}(q)|$ , Figure S11B shows that the sharp minimum shifts to a slightly higher  $q$  ( $0.41 \text{ nm}^{-1}$  vs  $0.38 \text{ nm}^{-1}$ ), and the intensity contribution is higher if the un-scaled data is used. Nevertheless, the two extracted  $|I_{cat}(q)|$  show reasonable agreement within the associated uncertainties. Furthermore, as discussed above, the scaled data makes more physical sense. Therefore, we have used these processed data sets for analyzing the distribution of counterions surrounding SNA-AuNP.

Up until now, we have extracted  $I_{cat}(q)$  by a combined analysis of the SAXS intensity profiles from SNA-AuNP in 4 MCl solutions. Here, we show that the low  $q$  ( $q \sim 0.4 \text{ nm}^{-1}$ ) minima in  $I_{cat}(q)$  are inherent in the raw SAXS data. To this end, we extract  $I_{cat}(q)$  from the un-scaled SAXS profiles from SNA-AuNP in 30 and 50 mM solutions of each of the 4 MCl (Figure

S12). Specifically,  $I_{cat,M}(q) = \{\Delta I_M(q) - [F_{np}(q)]^2\} / \Delta f_M$ . Here,  $\Delta I_M(q)$  is the scattered intensity from SNA-AuNP in a given MCl solution, above the background solution scattering.  $[F_{np}(q)]^2$  is the SAXS-extracted cation-independent intensity obtained by the linear fit procedure outlined in the main text. For the case of SNA-AuNP in the 30 mM solutions,  $[F_{np}(q)]^2$  is shown in Figure S11A (dotted red line). Finally,  $\Delta f_M$  is the effective number of electrons for a given cation M (Table S1).

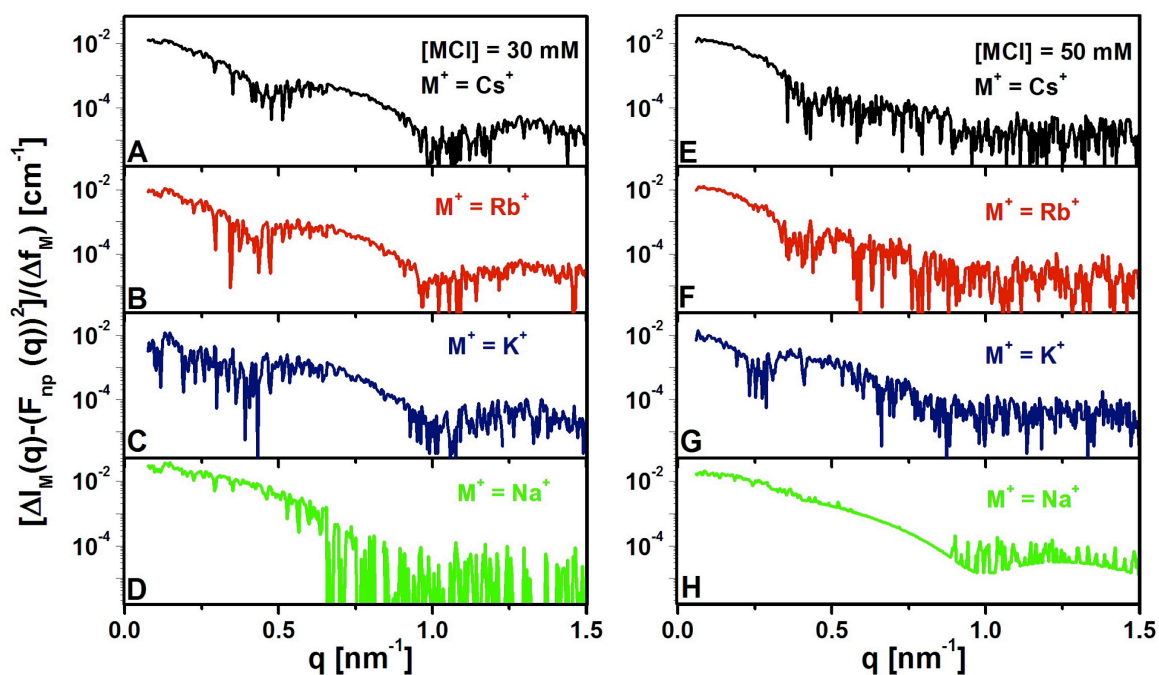


**Figure S12.** Extracted  $|I_{cat}(q)|$  from the as collected data for SNA-AuNP in 30 mM and 50 mM MCl. (A) and (E) 30 and 50 mM CsCl, respectively, (B) and (F) 30 and 50 mM RbCl, (C) and (G) 30 and 50 mM KCl, and (D) and (H) 30 and 50 mM NaCl, respectively.

Figure S12 shows that all  $I_{cat}(q)$  intensity profiles with the exception of those for SNA-AuNP in NaCl, clearly show the presence of a low  $q$  minimum. It should be noted that the scattered intensity from SNA-AuNP in NaCl, even at  $q = 0$ , is expected to differ from  $[F_{np}(q)]^2$  by only  $\sim 2 \times 0.5\% = 1\%$ . Where, 2% is the change expected on the basis of model HIRSAXS calculations (section II, above) and 0.5 is the approximate scale factor  $SF$ . Therefore, small

deviations of the data points from the best-fit lines (obtained by fitting the 4  $[\Delta I_M(q) \text{ vs } \Delta f_M]$  points at each  $q$ ) most sensitively affect the extracted  $I_{cat}(q)$  profiles in this case. In fact, the oscillations in  $I_{cat}(q)$  for the case of SNA-AuNP in NaCl solutions can be recovered by forcing an  $\sim 1\%$  change in  $[F_{np}(q)]^2$  (not shown). Similar to the case of SNA-AuNP in NaCl, small deviations cause the minimum position to not be coincident for the cases of SNA-AuNP in CsCl, RbCl, and KCl. The variations in  $I_{cat}(q)$  extracted from the 4 individual SAXS profiles illustrates one of the causes for the large error bars in the extracted  $I_{cat}(q)$  from the combined analysis. Nevertheless, Figure S12 shows that the oscillations in the extracted  $I_{cat}(q)$  were truly present in the original datasets. Further, the above observations validate our strategy of using 4 different MCl solutions in extracting the cation-independent and the cation-dependent SAXS intensities.

### **XIII. Note on form-factor for spherically symmetric objects**

The section on Guinier analysis (Pg. 137, Reference 13) shows that for  $q \rightarrow 0$ , the scattering amplitude from a solid homogenous sphere has the form  $F(q) = [A - B(q^2/10)]$ . It can be shown that the same function form holds for any spherically symmetric object. Consider a spherical object that is described by a core of radius  $R_c$ , volume  $V_c$ , and electron density  $\rho_c$  and is surrounded by  $m$  shells of thicknesses  $t_i$ , electron densities  $\rho_i$  and volumes  $V_i$ . Here, the shell number  $i$  varies from 1 to  $m$ , with a higher shell number corresponding to a larger separation from the core. The scattering amplitude from such an object for  $q \rightarrow 0$  can be written as  $F(q) = V_c(\rho_c - \rho_1)(1 - q^2 R_c^2/10) + (V_c + V_1)(\rho_1 - \rho_2)(1 - q^2(R_c + t_1)^2/10) + \dots\dots\dots(V_c + V_1 + \dots\dots + V_m)(\rho_m - \rho_s)(1 - q^2(R_c + t_1 + \dots\dots + t_m)^2/10)$ , where  $\rho_s$  is the electron density for the solution in which such objects are dispersed.

## References and Notes

1. Andresen, K.; Das, R.; Park, H. Y.; Smith, H.; Kwok, L. W.; Lamb, J. S.; Kirkland, E. J.; Herschlag, D.; Finkelstein, K. D.; Pollack, L. Spatial Distribution of Competing Ions around DNA in Solution. *Phys. Rev. Lett.* **2004**, *93*, 248103.
2. Das, R.; Mills, T. T.; Kwok, L. W.; Maskel, G. S.; Millett, I. S.; Doniach, S.; Finkelstein, K. D.; Herschlag, D.; Pollack, L. Counterion Distribution around DNA Probed by Solution X-Ray Scattering. *Phys. Rev. Lett.* **2003**, *90*, 188103.
3. Dingenouts, N.; Merkle, R.; Guo, X.; Narayanan, T.; Goerigk, G.; Ballauff, M. Use of Anomalous Small-Angle X-Ray Scattering for the Investigation of Highly Charged Colloids. *J. Appl. Crystallogr.* **2003**, *36*, 578-582.
4. Dingenouts, N.; Patel, M.; Rosenfeldt, S.; Pontoni, D.; Narayanan, T.; Ballauff, M. Counterion Distribution around a Spherical Polyelectrolyte Brush Probed by Anomalous Small-Angle X-Ray Scattering. *Macromolecules* **2004**, *37*, 8152-8159.
5. Lee, O.-S.; Prytkova, T. R.; Schatz, G. C. Using DNA to Link Gold Nanoparticles, Polymers, and Molecules: A Theoretical Perspective. *J. Phys. Chem. Lett.* **2010**, *1*, 1781-1788.
6. Gelbart, W. M.; Bruinsma, R. F.; Pincus, P. A.; Parsegian, V. A. DNA-Inspired Electrostatics. *Phys. Today* **2000**, *53*, 38-44.
7. Hill, H. D.; Millstone, J. E.; Banholzer, M. J.; Mirkin, C. A. The Role Radius of Curvature Plays in Thiolated Oligonucleotide Loading on Gold Nanoparticles. *ACS Nano* **2009**, *3*, 418-424.
8. Hefferan, K.; O'Brien, J. *Earth Materials*; Wiley-Blackwell: Chichester, U.K.; Hoboken, NJ, 2010.
9. CRC Handbook of Chemistry and Physics, 52nd ed.; CRC Press: Cleveland, Ohio, 1977.

10. Hurst, S. J.; Lytton-Jean, A. K. R.; Mirkin, C. A. Maximizing DNA Loading on a Range of Gold Nanoparticle Sizes. *Anal. Chem.* **2006**, *78*, 8313-8318.
11. Baldino, F.; Chesselet, M. F.; Lewis, M. E. High-Resolution *In Situ* Hybridization Histochemistry. *Methods Enzymol.* **1989**, *168*, 761-777.
12. Freeman, G. S.; Hinckley, D. M.; de Pablo, J. J. A Coarse-Grain Three-Site-Per-Nucleotide Model for DNA with Explicit Ions. *J. Chem. Phys.* **2011**, *135*, 165104.
13. Als-Nielsen, J.; McMorrow, D. *Elements of Modern X-Ray Physics*. 2nd Ed.; John Wiley: Chichester, U.K., 2011.